Digital Carbonate Rock Physics

Erik H. Saenger[1,2], Stephanie Vialle[3], Maxim Lebedev[3], David Uribe[2,4], Maria Osorno[2,4], Mandy Duda[1], and Holger Steeb[4,5].

[1]International Geothermal Centre, 44801 Bochum, Germany
[2]Ruhr-Universität Bochum, 44801 Bochum, Germany
[3]Curtin University, Perth, Australia
[4]University of Stuttgart, 70569 Stuttgart, Germany
[5]Stuttgart Research Centre for Simulation Technology (SRC SimTech), 70569 Stuttgart, Germany

Correspondence to: E. H. Saenger (erik.saenger@rub.de)

Abstract. Modern estimation of rock properties combines imaging with advanced numerical simulations, an approach known as Digital Rock Physics (DRP). In this paper we suggest a specific segmentation procedure of X-Ray micro-Computed Tomography data with two different resolutions in the μm-range for two sets of carbonate rock samples. These carbonates were already characterized in detail in a previous laboratory study which we complement with nano-indentation experiments (for local elastic properties). In a first step a non-local mean filter is applied to the raw image data. We then apply different thresholds to identify pores and solid phases. Because of a non-neglectable amount of unresolved micro-porosity ("micritic phase") we also define intermediate threshold values for distinct phases. Based on this segmentation we determine porosity-dependent values for effective P- and S-wave velocities as well as for the intrinsic permeability. For effective velocities we confirm an observed two-phase trend reported in another study using a different carbonate dataset. As an upscaling approach we use this two-phase trend as an effective medium approach to estimate the porosity-dependent elastic properties of the micritic phase for the low-resolution images. The porosity measured in the laboratory is then used to predict the effective rock properties from the observed trends for a comparison with experimental data. The two-phase trend can be regarded as an upper bound for elastic properties; the

use of the two-phase trend for low-resolution images lead to a good estimate for a lower bound of effective elastic properties. Anisotropy is observed for some of the considered subvolumes, but seems to be insignificant for the analysed rocks at the DRP scale. Because of the complexity of carbonates we suggest to use DRP as a complementary tool for rock characterization in addition to classical experimental methods.

1 Introduction

Three-dimensional information on rock microstructures is important for a better understanding of physical phenomena and for rock characterization on the micro-scale. Various destructive and non-destructive methods for obtaining a 3D image of the rock microstructure exist (Arns et al. 2002; Saenger et al. 2004; Madonna et al., 2013, Cnudde and Boone, 2013, and references therein). The most common non-destructive 3D imaging technique for rock samples is X-Ray Computed Tomography (XRCT). A common problem, however, is a clear trade-off between sample size and resolution. For each material a specific, and large enough, sample size is required to ensure that the selected volume is representative of the physical property to be computed (e.g., Hill 1963; Costanza-Robinson et al. 2011; Andrä et al. 2013a). It can, however, be at the expense of a lost of pore features resolution. In the last decade, the X-Ray micro-Computed Tomography (micro-XRCT) method became widely available and many modern studies have made use of it to obtain 3D rock images (e.g., Fusseis et al. 2014). The resolution of micro-XRCT of up to $(0.6\ \mu m)^3$ (voxel size) is high enough to image the spatial distribution of grains, pores, and pore fluids for a wide variety of rocks (e.g., Blunt et al. 2013; Madonna et al. 2013).

Rock images from 3D XRCT can be used for predicting properties such as porosity, permeability, pore size distribution, effective elastic moduli, or electrical conductivity (e.g., Andrä et al. 2013b). For example, Darcy permeability can be predicted by numerically simulating single-phase fluid flow through 3D rock pore structure models, with the numerical results being in reasonable agreement with laboratory measurements (e.g., Osorno et al. 2015, Saenger et al. 2016). In this case, the resolution of the micro-XRCT technique is sufficient, because fluid pathways predominantly follow larger pores. However, if the pore size is much smaller than 1μm the agreement might be less satisfactory due to

2

resolution limitations. On the other hand, mechanical properties, such as the effective elastic moduli, strongly depend on the microstructural details of the rock, which may stay unresolved by the micro-XRCT technique (e.g. for Bentheim sandstone considered in Saenger et al., 2016). The inability to fully characterize the microstructural details of a rock sample can lead to a disagreement between numerical estimates of mechanical properties based on micro-XRCT images and laboratory data (Andrä et al. 2013b).

An example of such a disagreement between laboratory and Digital Rock Physics (DRP) estimates is described in Andrä et al. (2013a,b). In these benchmark papers a comparison between different numerical methods is presented. All DRP estimates of the effective elastic bulk modulus use the same segmented dataset. Regardless of the numerical approach all computational predictions overestimate the bulk modulus measured in the laboratory. This conclusion is mostly based on Berea sandstone although carbonates are considered in this study. However, also Jouini et al. (2015) reports about an overestimation of effective elastic properties of carbonates by DRP. Therefore we conclude here that the digital rock images themselves and/or the computational workflow have to be improved to provide better estimates of effective properties of rocks. In this paper we consider in detail a carbonate dataset and suggest techniques to achieve a better agreement between numerical predictions and laboratory measurements. Our study is complementary to the DRP-carbonate studies performed in Derzhi et al (2010), Lopez et al. (2012), Ringstad et al. (2013), Andrä et al. (2013a,b) and Jouini et al. (2015). In contrast to these studies our Digital Rock Physics study is complemented with a very detailed experimental characterization (section 2). Our suggested segmentation technique (section 3) is used to estimate effective mechanical as well as effective transport properties (section 4). Among others, we observe a two-phase trend for mono-mineralic (calcite) carbonates which can be regarded as an upper bound for velocities at all scales (see discussion in section 5) due to the observed self-similarity of those rocks (Jouini et al. 2015).

2 Rock Samples and Laboratory Characterization

2.1 Carbonate samples

We studied samples of two carbonates from the Upper Cretaceous carbonate system of the Gargano-Murge region (Southern Italy). *Carb-A* is a limestone from the Paleocene-Eocene Peschici formation, and *Carb-B* is a micritic mudstone from the Late Cretaceous Monte Acuto formation (Martinis and Pavan, 1967; Cremonini et al., 1971). Both carbonates are composed of nearly 100 % calcite (Scotallero et al., 2014).

Both samples have been characterized in the laboratory in detail in Vialle et al. (2013); e.g. SEM images showing the microstructure of these two samples. We give here only a short summary. Both carbonate samples display a matrix of micrite (abbreviation for *micr*ocrystalline calc*ite*) whose grain size is typically 1–4 μm (Moshier, 1989), but the texture of these micrites is different between the two samples. Following the classification of micrite microtexture proposed by Lambert et al. (2006) and Deville de Periere et al. (2011), the micrite in sample *Carb-A* is mainly a "tight micrite", spatially varying from anhedral compact to fused, with grains typically 1–2 μm in diameter; micrite in sample *Carb-B* is a "porous micrite" varying from rounded to subrounded, with anhedral to subhedral, rounded grains, typically 2–4 μm in diameter. Beside a micrite matrix, sample *Carb-A* exhibits vuggy-like pores either rounded, up to about 60μm, or more elongated, up to 300 μm in length. Sample *Carb-B* exhibits a spar calcite cement of grains typically 10 to 100's of micrometers in diameter, as well as rounded vugs up to about 100–200 μm.

He-grain density, bulk density and resulting porosity, as well as air-permeability, were previously measured at room pressure and temperature on core plugs 1'' (0.025 m) in length and diameter (Vialle et al., 2013). The associated errors did not exceed 0.5 %, 1 %, and 2 %, respectively. P- and S-wave velocities, at 1 and 0.7 MHz frequency, respectively, were acquired on dry samples under increasing (up to 30 MPa) and decreasing hydrostatic stress. Velocities were measured by using a pulse-transmission technique. The errors in V_P and V_S are about 1 %. The results are listed in Tables 1 and 2. The obtained grain densities (2690 ± 10 kg/m^3 and 2700 ± 10 kg/m^3, for samples *Carb-A* and *Carb-B*, respectively) are in agreement with a mineralogy of pure calcite (Mavko et al., 2009).

4

2.2 Nano-indentation

Nanoindentation tests were performed to obtain stiffness (Young's modulus) of the carbonates at the micrometer-scale. These tests were performed on room-dried samples consisting of two small irregular pieces, about 5 mm thick and with a surface of a few cm^2, taken from the cuttings of the 1'' core plugs of *Carb-A* and *Carb-B*. Prior to testing, the surface of each sample was polished with carbide paper (grit 120). Roughness (Sq) of the surface measured by DS 95 AFM system (Semilab) on 10 μm x 10 μm areas was 1.4 μm (RMS values) for *Carb-A* and not measured for *Carb-B*. The IBIS nano-indentation system (Model B, Fisher-Crips Laboratories Pty.Ltd.) is equipped with a Berkovich-type diamond indenter (Lebedev et al, 2014) and was used in a static mode: the tests consist in continuously recording the load, *P,* and the displacement, *h,* of the indenter as it pushes into and withdraws from the surface of the sample. A constant maximum loading force of 10mN and an initial contact force of 0.15 mN were used. In total, 961 (31 x 31) measurements were performed on a 300 x 300 μm surface with a spacing of 10μm between measurement points.

Typically, the extraction of the mechanical properties is achieved by using the *P-h* curves and by applying a continuum scale mechanical model to obtain the indentation modulus *M* (Fischer-Cripps 2004, Lebedev et al. 2014):

$$M \overset{def}{=} \frac{\sqrt{\pi}}{2} \frac{S}{\sqrt{A_c}} \tag{1}$$

where *S* the is unloading indentation stiffness $S = \left(dP/dh \right)_{h=h_{max}}$ and A_c the contact area, extrapolated from the maximum penetration depth h_{max} and using the relation $A_c = 24.5 \ h_{max}^2$ according to the geometry of Berkovitch-type indenters (Fischer-Cripps 2004).

Data was further corrected considering deviation of the indenter tip from ideal geometry, initial penetration into the rock below a load threshold and compliance of the loading column, leading to a nominal uncertainty of indentation moduli of < 2 GPa.

Young's moduli , *E,* can be calculated from the indentation moduli (Fischer-Cripps 2004) according to

$$\frac{1}{M} = \frac{1-v^2}{E} + \frac{1-v_i^2}{E_i} \quad . \tag{2}$$

Indenter properties are E_i= 1220 GPa and ν_i = 0.06, according to Klein & Cardinale (1992) and Fischer-Cripps (2004), for diamond material. Each performed measurement covers a projected surface of about 40μm² on average (which corresponds to an equilateral triangle with a side of 6μm), and contains both pores and solid grains. A Poisson's ratio has also to be assumed for each nano-indentation measurement: even though we can compute it from the laboratory ultrasonic P- and S- wave measurements at the core scale, there is no reason to assume that this value is constant for each individual measurement. This local Poisson's ratio cannot be measured experimentally and we have taken here a constant value of 0.3. Figure 1 displays the distribution of the indentation moduli for both *Carb-A* (left) and *Carb-B* (right).

3 The CT-datasets

3.1 Procedure to get CT-Images

Two samples were prepared for imaging with micro-XRCT from the cuttings, one from *Carb-A* and one from *Carb-B*. A cylindrical-shape sample of 1.5cm in height and 2mm in diameter was achieved by gently grinding the cuttings, first on the side on a rock saw blade, and then by hand using sand paper (grit 120). This procedure allows obtaining very thin cylinders while minimizing mechanical damage that classical drilling would produce. These cylindrical samples were then glued with Crystalbond509 (SPI suppliers) on a 2mm diameter flat-head metal pin, which was itself inserted in the core holder of the micro-tomograph. The 3D X-ray Microscope Versa XRM 500 (Zeiss - XRadia) was used with a X-ray energy of 60 keV. Two different settings of source-to-sample and detector-to-sample distance were used to achieve two nominal voxel sizes of $(3.4 \ \mu m)^3$ and $(0.6 \ \mu m)^3$ for *Carb-A*, and of $(3.4 \ \mu m)^3$ and $(1.1\mu m)^3$ for *Carb-B*, referred to as "low" resolution and "high" resolution, respectively, for each for the two samples. X-ray microscope and image acquisition settings are summarized in Table 3 for each of the two samples.

The number of radiographic projections acquired during sample imaging with "low" and "high" resolutions were 3001 and 5001, respectively. The total scanning time for one sample was about 8h. Initial cone-beam 3D image reconstruction was performed using the internal software XM

6

Reconstructor (XRadia). To remove geometrical artefacts during reconstruction a secondary reference was acquired for samples image with maximum resolution.

3.2 Segmentation procedure

In addition to solid grains and pore space different micritic phases are visible in the raw images of the scans entailing an advanced segmentation procedure. For our segmentation (Figure 2) we select a region of interest (ROI) from the raw data of the two types of carbonates with two different resolutions (Tab 3). The ROI is subdivided in eight partly overlapping subvolumes, each of a size of 400^3 voxels (Figures 3 and 4). For the low-resolution images, it gives thus eight cubes with a side of 1.37 mm for both samples, and for the low-resolution images, 8 cubes with a side of 0.25 mm for *Carb-A* and of 0.46 mm for *Carb-B*.

Our segmentation workflow is applied to the full ROI including all subvolumes. Image enhancement and segmentation steps were carried out using the software package Avizo Fire 9 (FEI Visualization Sciences Group). Before actual segmentation the image noise and scan artefacts are reduced while preserving interfaces using a 3D non-local mean image filter. To our experience the standard values of this filter are appropriate (Search Windows = 21; Local Neighborhood = 5; Similarity Value = 0.6). Note that every step of image enhancement changes the original data set affecting subsequent steps required for data analysis.

The image-enhanced datasets were segmented into classes using global thresholds for the covered range of grey-values. The global threshold is valid for all the eight partly overlapping subvolumes mentioned above. Considering that the samples represent quasi monomineralic calcitic rocks we identified the following classes illustrated in Figures 5 and 6:

- high-confidence pores (illustrated with dark blue color),
- high-confidence mineral (illustrated with dark red color),
- and five intermediate classes.

Note that a non-negligible part of the pore space is below the resolution limit of the μ-CT scans (cf. results of mercury intrusion showing pores and pore throats as low as 0.06 μm, Figure 6 of Vialle et al. (2013). We found that five intermediate classes are sufficient to describe the calcitic rocks used in this

7

study, but the number of classes between the high-confidence mineral class and the high-confidence pore class can be increased or decreased for other materials. In contrast to Lopez et al. (2012) or Ringstad et al. (2013) we do not think that the density can be approximated directly by the grey value of those micritic phases. From our point of view the relationship between grey-value and density can be highly non-linear and becomes even more complicated in the case of multi-mineral rocks. However, we make use of the accepted assumption that lighter grey values in the histogram correspond to lower porosities.

4 Numerical Results

In order to numerically calculate the effective intrinsic permeability k of the digitized rock sample we calculate the fluxes under creeping flow condition based on a parallelized Stokes-solver. The parallelized Finite Difference-based Stokes-solver is suitable for the calculation of effective hydraulic parameters for low and high porous materials (cf. Osorno et al., 2015). Using volume averaging technique, we coarse-grain the local velocity field $\boldsymbol{u}(\boldsymbol{x})$ obtaining the global velocity component u_m in flow direction.

The intrinsic permeability k is calculated with Darcy's law:

$$k = \frac{\mu\, u_m}{\Delta p}. \qquad (3)$$

The pressure gradient Δp is imposed with pressure boundary conditions in the numerical simulations. The dynamic viscosity of the pore fluid is μ. In our numerical simulations Δp is -5.8 10-4 Pa/m and μ is 1.2 Pa.s.

To obtain effective P- and S-wave velocities of the digitized rock samples we use a technique described in detail in Saenger et al. (2011) and references therein. The basic idea of this approach is to study speeds of elastic waves through heterogeneous materials in the long wavelength limit (pore size $\ll$ wavelength) using the rotated staggered grid (RSG) finite-difference algorithm (Saenger et al., 2000) for the simulation of elastic wave velocities (cf. Andrä et al. 2013a,b).

4.1 High Resolution

4.1.1 Permeability

Permeability calculations were realized for subvolumes of the *Carb-A* and *Carb-B* samples. However, the domain size of the *Carb-A* (0.43 mm) and *Carb-B* (0.78 mm) high resolution samples is smaller than

5 the low resolution ones (2.4 mm for *Carb-A* and *Carb-B*), i.e. less representative of the material, therefore we numerically investigate only the extreme porosity configurations. To select the domains for permeability calculation we adapt the porosity configurations (range defined by high-confidence pores to high-confidence grains; see also discussion in section 5.2) showing the minimum and maximum deviation in porosity with respect to the experimental investigation. To analyse the

10 homogeneity of the sample this step was performed for all 8 subvolumes. For the high resolution subdomains (*Carb-A* and *Carb-B*) we perform Stokes flow simulations only in one direction (z-direction, cf. Figure 3).

Figure 7 left hand side displays the intrinsic permeability calculated for the *Carb-A* high resolution. The porosity range of the subvolumes is higher than the experimentally determined porosity. In addition, the

15 numerically calculated permeability values are significantly lower than the values obtained for the low-resolution samples. Figure 7 right hand side shows the results of the intrinsic permeability calculated for the selected high-resolution samples of the *Carb-B*. It can be observed, that the high-resolution sample show a much lower variation between the extreme values of the porosity range.

From the results of the high-resolution samples, *Carb-A* and *Carb-B*, it could be observed that the

20 variation in pores channels arrangement is significant and the permeability in the different subvolumes of the same material does not necessarily increase with the porosity increment.

4.1.2 Elasticity

Several micritic phases have been identified in the raw images of the carbonate rock (i.e. the phases between high-confidence pores and high-confidence minerals; compare with section 3.2). The porosity

25 of these regions cannot be determined exactly, as some pores are below the resolution of the scans: typically, micrites exhibit pore sizes with a maximum diameter of 1 μm (Moshier, 1989; Cantrell and Hagerty, 1999), and pore sizes as low as 0.06 μm have been measured by MICP for the samples under

investigation (Vialle et al., 2013). To account for the unresolved pore space we perform a number of two-phase wave-propagation simulations to estimate effective elastic properties (Saenger et al. 2004; Saenger et al. 2011; Saenger et al. 2016). For these time-of-flight simulations we assign vacuum properties to the pore phase, while the rest of the digital image including the micritic phase will be

5   assumed to be solid with the mineral properties of calcite (e.g. Andrae et al., 2013b). For the second simulation, we assign vacuum properties to the pores and the first micritic phase, while the rest will be assumed to be solid. We continue this way for all micritic phases, so that the last simulation assigns the mineral properties of calcite only to the high-confidence mineral phase. By this technique we obtain a porosity-velocity trend (Figure 8) for a random selection of high resolution subvolumes for *Carb-A* and

10 *Carb-B*:

$$Vp = 6259.1 \text{ m/s} - \phi * 9640 \text{ m/s} + 3381 \text{ m/s} * \phi^2 \qquad (4)$$

$$Vs = 3237.2 \text{ m/s} - \phi * 3237.2 \text{ m/s} \qquad (5)$$

This porosity-velocity trend is exactly the same as has been observed for a carbonate dataset from a different location used in Saenger et al. (2014). In their paper this trend has been observed for three

15 different resolutions (65 nm, 1 µm, 4 µm). Please note that due to computational restrictions we are only able to simulate a random selection of subsamples; however, as shown in Figure 8, all our calculated velocities follow the trends according to equations (4) and (5).

4.2 Low Resolution

4.2.1 Permeability

20 Similar to the procedure of the numerical simulation for elasticity (Section 4.1.2) we vary the sample porosity. This way we get six different porosities for each subvolume depending on the threshold variation. To reduce computational times for the Stokes flow simulation we eliminate the disconnected pores. Some subvolumes solid-pore configurations with the lower porosities do not present connected pores, and we assume for the effective permeability *k*=0.

25 Figure 9 present the permeability values for *Carb-A* (left hand side) and *Carb-B* (right hand side) samples as a function of porosity. For the permeability calculations for these samples we perform Stokes flow simulation in z-direction only (compare Figure 3).

10

Additionally we performed the Stokes flow simulations in three directions (X, Y and Z) for *Carb-A* sample (see Figure 11). From the simulation results it can be seen that the *Carb-A* sample permeability (Figure 11 left hand side) is anisotropic with a variation between directions of up to 80 %. In some subvolumes permeability value varies by up to two orders of magnitude.

5   From the CT data of the low resolution *Carb-A,* the largest domain that could be extracted is 2.4 mm x 2.4 mm x 2.4 mm (689^3 voxels). The permeability calculated for this domain is 13.0 D for a porosity of $\phi = 0.173$.

4.2.2 Elasticity

For the low-resolution scans we repeat the two-phase simulations for *Carb-A* and *Carb-B* as described
10 in section 4.1.2. The results are displayed in Figure 10. Interestingly, the two-phase trend given by Equations (4) and (5) is confirmed only clearly for S-wave velocities of *Carb-A* and *Carb-B*. For the case of P-wave velocities we observe a slightly different trend (cf. eq. (4)) that we illustrate with blue dashed-dotted lines in Figure 10:

$$Vp = 6259.1 \text{ m/s} - \phi * 7970 \text{ m/s} + 1700 \text{ m/s} * \phi^2 \qquad (6)$$

15 Especially in the low-resolution case we expect to have images with a large amount of unresolved porosity, mainly due to micritic phases. Therefore we perform multi-phase simulations and vary the porosity by assigning effective elastic properties to an interval of micritic phases (always starting with the class closest to the high-confidence pore phase). As effective medium approach we use the trend given by the simulations using two single phases only (Equations (4) and (5)), which is supported by
20 two observations. First, this trend was already observed by Saenger et al. (2014) on different scales on a different carbonate dataset. Second, there is an observed self-similarity for carbonates (Jouini et al. 2015). Therefore, despite the interval of micritic phases, we assign vacuum values for the high-confidence pores and use for the remaining phases the known elastic moduli of calcite (e.g. Andrae et al., 2013b). The results are displayed with green dots for *Carb-B* in Figure 10. We repeat the procedure
25 with different intervals of the micritic phases. There are three interesting observations: (1) the resulting effective velocities are always significantly below the observed two-phase trend, (2) the curves for

11

different intervals will intersect each other, and (3) the experimental determined velocities for high confining pressures are between the multi-phase results and the two-phase trend as described above.

5 Discussion

In this paper we compare results from laboratory investigations with numerical estimates based on digital images. Note that in laboratory experiments we use samples on the cm-scale for the determination of permeability and ultrasonic velocities and compare it with DRP-predictions based on images on the mm-scale. Especially because of the known heterogeneity of carbonates there is always a risk that the selected scanned area is not representative compared to the full sample size used for laboratory characterizations. In general, a multi-scale approach as suggested by Ringstad et al. (2013) should be used for upscaling the results to the plug scale. However, our studies on *Carb-A* and *Carb-B* suggest workflows which should be applied in practice for as many samples as possible for improving the statistical significance.

5.1 Discussion of Experimental Characterization

Even with the highest resolution currently available in micro-XRCT imaging there will be a significant amount of unresolved pore features which need to be treated in the DRP workflow (Saenger et al., 2016). On the grey-scale intensity level histograms of the low- and high-resolution images of the micro-CT scanning (Figure 5) this is reflected in a continuum in the intensity levels between the phase identified as pores and the phase identified as calcite grains. In this paper we have dealt with these micritic phases by replacing, step-by-step, and in a cumulative way, each of the micritic phases by void, and establishing a porosity-velocity trend. A more advanced technique using dry and wet imaging is suggested by Bhattad et al. (2014)using the difference imaging to approximate effective properties. However, the nano-indentation technique provides a measure for the distribution of effective elastic properties at the micrometer-scale, and can thus potentially constrain the input parameters for the different phases identified during the segmentation. To be able to do so, nano-indentation needs to provide bulk and shear moduli from each of the measurements (load-displacement curves) and we need to obtain effective bulk and shear moduli values for each of the identified phases in the micro-

12

tomography (pores, calcite grains and the five micritic phases). However, if nano-indentation technique is a well-established technique in material sciences, which deals with homogeneous, purely elastic materials, this is, as of today, not yet the case for rocks, which are heterogeneous materials with both elastic and non-elastic behaviour (creep). Though nano-indentation tests provide significant insights

5   into elastic properties of heterogeneous rocks such as carbonates (Lebedev et al., 2014; Vialle & Lebedev, 2015) or shale (Ulm & Abousleiman, 2006; Abousleiman et al., 2007), there are still some points to be looked at before using the derived values of Young's (or shear and bulk) moduli in a quantitative way for DRP: value of Poisson's ratio to be used, effect of surface roughness, local mechanical damage induced on the sample's surface by polishing techniques, etc. Nonetheless, the

10 histograms of the indentation moduli of both samples show a broad distribution of moduli values ranging from very low values (a few GPa, where the indenter tip measures stiffness of an area mostly made of a pore) to values consistent with calcite. The existence of these intermediate values is consistent with the existence of micritic phases identified with X-ray tomography. However, we did not observe two peaks in the histogram for the nano-indentation results (Figure 1) in contrast to the

15 histograms of the scanned micro-XRCT-images (Figure 5). Therefore the direct translation of moduli derived from nano-indentation remains also difficult. The "resolution" of nano-indentation used in this study allows for determining effective elastic properties at slightly bigger scales than that used here for the micro-XRCT.

Regnet et al. (2014) showed that there is a relationship between micrite microstructure and laboratory

20 ultrasonic velocities on core samples, with samples with higher content of 'tight micrite' exhibiting higher velocities and samples with higher content of 'microporous micrite' exhibiting lower velocities. Studied core samples were though a mixture of different types of micrite and the measured velocities represent effective properties at the core scale. This observation is reflected in the established porosity-velocity trends (Equations 4, 5 and 6): micritic phases with density closer to that of calcite ('tight

25 micrites') have higher velocities than micritic phases with lower density (Figures 8 and 10) closer to that of pores ("microporous micrites').

13

5.2 Discussion of Porosity: Experiments vs. Digital Rock Physics

After the segmentation it is also possible to estimate the porosities of the samples. Based on the suggested workflow described in section 3.2 there will be a lower and upper bound. For the lower bound we will treat only the "high-confidence pores" as pores; for the upper bound we count only "high-confidence minerals" as minerals.

We obtain a porosity range between 25 % and 35 % for the high-resolution data of *Carb-A* and a range between 7.5 % and 31 % for the low-resolution data. We observe that the mean value is in rough agreement with the experimentally determined porosity of 16.7 % (see Table 1) only for the low-resolution case. Although also the experimental value comes with an error we conclude that the high-resolution dataset for *Carb-A* is maybe not representative for the full sample used for the helium porosity in the laboratory. In case of *Carb-B* the intervals range from 13 % to 45 % and 7 % to 48 % for the high-resolution and low-resolution case, respectively. Here the mean value is in both cases closer to the experimentally determined porosity of 29.4 %.

We conclude that the porosity values of carbonates using micro-XRCT data will only provide estimates with a relatively high uncertainty due to the significant amount of unresolved pore features in the images. An indication is the result of the mercury-intrusion experiments presented by Vialle et al. (2013): the pore throats of the micritic phase are mainly below the resolution of available micro-XRCT devices.

5.3 Discussion of Permeability: Experiments vs. Digital Rock Physics

Permeability numerically estimated for *Carb-B* (Figure 9 right hand side) presents an error of 97 % on average with respect to the experimental value. In some cases the error is as low as 55 %. The numerical error in comparison with the experimental values is within the expected range for the numerical method at these porosities, cf. Table 1 in Osorno et al. (2015).

Experimental results for *Carb-A* sample are below the measurement error tolerance. This could imply a sample with no connected pores between the inlet and outlet defined for the experiment. The numerical estimation of the permeability for the *Carb-A* low resolution sample (Figure 9 left hand side) is four orders of magnitude higher than the experimental measurement (on average 7.0 D). In the high

14

resolution case (Figure 7 left hand side) the numerical estimation is closer to experimental results (on average 0.1 D), but the porosity presents a large numerical error, therefore we do not take this domain as representative of the sample. However the numerically calculated permeability does not differ much from values found in the literature for porous rocks with alike porosity (cf. Andrä et al., 2013b). On the

5   other hand it is observed that for a porosity below 25 % permeability values of carbonates can span several orders of magnitudes (e.g. Figure 3 of Vialle et al. 2013). Therefore we suggest considering a statistically significant number of samples to characterize a formation and found that 8 samples are sufficient for the numerical permeability calculations (see Figures 7 and 9).

5.4 Discussion of Elasticity: Experiments vs. Digital Rock Physics

10   There are two important observations. The two-phase trend (displayed with solid and dashed-dotted lines) seems to be an upper bound for velocities. This data-driven upper bound is much stricter than the bound given by Hashin-Shtrikman (see Figure 8) and is now confirmed for several carbonates using several resolutions (this study and Saenger et al. 2014). Only for the low resolution images we observe a slightly different trend for for P-waves (equation (6) and Figure 10).

15   The trend given by the envelope of the multi-phase simulations (displayed by dashed-dotted lines in Figure 10; right hand side) is not a strict lower bound, because the shape will strongly depend on the applied method to determine effective elastic properties for areas which are below the resolution limit of the used XRCT-technique. The best choice to our knowledge is the two-phase trend discussed above, which can be regarded as a carbonate-data-driven effective medium approach. We suggest

20   implementing here in the future also the findings of the nano-indentation experiments. However, we observe that the velocities obtained for the multi-phase simulations are in a reasonable agreement with laboratory measurements. This is the case for a known porosity determined in complementary laboratory studies (see also section 5.1). For carbonates the distribution of the micritic phases and their effective elastic behavior is crucial to predict the effective wave speeds.

5.5 Discussion of Anisotropy: Elasticity vs. Permeability

In general we don't observe any significant anisotropy for permeability and for velocities of the considered samples. However, a few samples are out of this general trend. One example is a subvolume of *Carb-A* (low-resolution case), for which we show the results for P-wave velocities and permeabilities in Figure 11. Interestingly, the moderate anisotropy for the permeability is not present for the velocity.

6 Summary

With the current imaging techniques it remains difficult to resolve microstructures (on sub-micrometer scale) and image a representative volume at the same time, which is essential to understand the effective material properties of rocks. For this purpose the exact determination of the porosity of the rock samples is the most relevant parameter. To overcome this problem, we have conducted a specific multi-phase segmentation technique and a careful calibration of DRP estimates with laboratory data. Especially for carbonate samples it is difficult to estimate exactly the porosity from raw-CT data, because the micritic phases remain unresolved with an unknown porosity. Therefore, we use our presented numerical results in an inverse way. We suggest using the porosity determination from the laboratory and go back to our low-resolution trends given in Figure 9 and 10. With a given porosity we can now estimate the permeability and the effective wave velocities.

In case of the studied samples *Carb-A* and *Carb-B*, we can predict P- and S-wave velocities with a good agreement to laboratory results. The presented two-phase trend (Equations 4, 5 and 6) is found to be an upper bound for a wide range of scales and can also be used as an effective medium approach to the micritic phases. The predicted permeability values are only in good agreement for *Carb-B*. Most probably the low-resolution image of *Carb-A* is not representative for the sample used in the laboratory. However, for the used carbonate rock samples anisotropy seems insignificant for elastic as well as for hydraulic properties.

In general, the resolution of the XRCT is the limiting factor for the application of DRP for carbonate rock. The micritic phases remain unresolved even for the highest resolutions available. Therefore, the effective elastic properties have to be approximated. Our suggestion is to use the trend of the two-phase

16

simulations. The implemented workflow in this paper can be applied in general for numerical estimates of mechanical and transport properties of carbonates. Because of the known strong heterogeneity of carbonates we suggest to use a statistically significant amount of digital images to characterize a formation.

5   Acknowledgements

References

Abousleiman, Y.N.; Tran, M.H.; Hoang, S.; Bobko, CP; Ortega, A; Ulm, F.J.: Geomechanics field and laboratory characterization of the Woodford Shale: The next gas play.SPE Annual Technical Conference and Exhibition, 2007.

Andrä, H.; Combaret, N.; Dvorkin, J.; Glatt, E.; Han, J.; Kabel, M.; Keehm, Y.; Krzikalla, F.; Lee, M.; Madonna, C.; Marsh, M.; Mukerji, T.; Saenger, E. H.; Sain, R.; Saxena, N.; Ricker, S.; Wiegmann, A. and Zhan, X.: Digital rock physics benchmarks-Part I: Imaging and segmentation. Computer & Geosciences 50, 25–32, 2013a.

Andrä, H.; Combaret, N.; Dvorkin, J.; Glatt, E.; Han, J.; Kabel, M.; Keehm, Y.; Krzikalla, F.; Lee, M.; Madonna, C.; Marsh, M.; Mukerji, T.; Saenger, E. H.; Sain, R.; Saxena, N.; Ricker, S.; Wiegmann, A. and Zhan, X.: Digital rock physics benchmarks-Part II: Computing effective properties. Computers & Geosciences, 50, 33-43, 2013b.

Arns, C. H.; Knackstedt, M. A.; Pinczewskiz, M. V. and Garboczi, E. J.: Computation of linear elastic properties from microtomographic images: Methodology and agreement between theory and experiment. Geophysics, 67, 1396-1405, doi: 10.1190/1.1512785, 2002.

Bhattad, P.; Young, B.; Berg, C.F.; Rustad, A.B. and Lopez, O.: X-ray micro-ct assisted drainage rock
5 typing for characterization of flow behaviour of laminated sandstone reservoirs: International Symposium of the Society of Core Analysts, Avignon, France, SCA2014-024, 2014.

Blunt, M.J, ; Bijeljic, B.; Dong, H.; Gharbi, O.; Iglauer, S.; Mostaghimi, P.; Paluszny, A. and Pentland, C.: Pore-scale imaging and modelling: Advances in Water Resources, 51, 197-216, DOI: 10.1016/j.advwatres.2012.03.003, 2013.

10 Cantrell, D.L. and Hagerty, R.M.: Microporosity in Arab Formation Carbonates, Saudi Arabia. GeoArabia, 4, No. 2, 1999.

Cnudde, V., and Boone, M. N.: High-resolution X-ray computed tomography in geosciences: A review of the current technology and applications. Earth Science Reviews, 123, 1-17, doi:10.1016/j.earscirev.2013.04.003, 2013.

15 Costanza-Robinson, M.S.; Estabrook, B.D. and Fouhey, D.F. Representative elementary volume estimation for porosity, moisture saturation, and air-water interfacial areas in unsaturated porous media: Data quality implications. Water Resources Research, 47, WO7513:1–WO7513:12, 2011.

Cremonini, G.; Elmi, C. and Selli, R.: Note illustrative della carta geologica d'Italia. Foglio 156 "S. Marco in Lamis": Servizio Geologico d'Italia, 1971.

20 Derzhi, N., Dvorkin, J., Diaz, E.,Baldwin, C., Fang, Q., Sulayman, A., Soroka, W. L., Clark, A., Al Dayyni, T. and Kalam, Z: Comparison of traditional and digital rock physics techniques to determine the elastic core parameters in Cretaceous formations, Abu Dhabi. Abu Dhabi International Petroleum Exhibition & Conference, Abu Dhabi, UAE, SPE-138586-PP, 2010.

Deville de Periere, M.; Durlet, C.; Vennin, E.; Lambert, L.; Bourillot, R.; Caline, B. and Poli, E.:
25 Morphometry of micrite particles in cretaceous microporous limestones of the Middle East: Influence

on reservoir properties. Marine and Petroleum Geology, 28, 1727–1750, doi: 10.1016/j .marpetgeo.2011.05.002, 2011.

Fischer-Cripps, A.C.: Nanoindentation, 2nd edition. Springer-Verlag. ISBN 0387220453, 2004.

Fusseis, F., Xiao, X., Schrank, C., and De Carlo, F.: A brief guide to synchrotron radiation-based microtomography in (structural) geology and rock mechanics. Journal of Structural Geology. Journal of Structural Geology, 65(C), 1–16, doi: 10.1016/j.jsg.2014.02.005, 2014.

Hill, R.: Elastic properties of reinforced solids: some theoretical principles. Journal of the Mechanics and Physics of Solids, 11, 357-372, 1963.

Jouini, M.S.; Vega, S. and Al-Ratrout, A.: Numerical estimation of carbonate rock properties using multiscale images. Geophysical Prospecting, 63, 405–421 doi: 10.1111/1365-2478.12156, 2015.

Klein, C.A. and Cardinale, C.F.: Young's modulus and Poisson's ratio of CVD diamond. Diamond and Related Materials, 2(5–7), 918-923, 1992.

Lambert, L.; Durlet, C.; Loreau, J. P. and Marnier, G.: Burial dissolution of micrite in Middle East carbonate reservoirs (Jurassic-Cretaceous): Keys for recognition and timing. Marine and Petroleum Geology, 23, 79–92, doi: 10.1016/j.marpetgeo.2005.04.003, 2006.

Lebedev, M.; Wilson, M.E.J., and Mikhaltsevitch, V.:An experimental study of solid matrix weakening in water-saturated Savonnières limestone. Geophysical Prospecting, 62, 1253-1265, doi: 10.1111/1365-2478.12168, 2014.

Lopez, O.; Mock, A.; Øren, P. E.; Long, H.; Kalam, Z.; Vahrenkamp, V.; Gibrata, M.; Seraj, S.; Chacko, S.; Al Hammadi, M.; Al Hosni, H.; Sahn, H. and Vizamora, A.: Validation of fundamental carbonate reservoir core properties using digital rock physics, *International Symposium of the Society of Core Analysts held in Aberdeen, Scotland, UK,* SCA2012-19, 2012.

Mavko, G.; Mukerji, T. and Dvorkin, J.: The rock physics handbook. Cambridge University Press, 2009.

19

Madonna, C.; Quintal, B.; Frehner, M.; Almqvist, B. S. G.; Tisato, N.; Pistone, M.; Marone, F. and Saenger, E. H.: Synchrotron-based X-ray tomographic microscopy for rock physics investigations. Geophysics 1, Vol. 78, D53-64, 2013.

Martinis, B., and Pavan, G.: Note illustrative della carta geologica d'Italia, Foglio 157 "Monte S.
5   Angelo": Servizio Geologico d'Italia, Roma, 1967.

Moshier, S. O.: Microporosity in micritic limestones: A review. Sedimentary geology, 63, 191–213, doi: 10.1016/0037-0738(89)90132-2, 1989.

Osorno M., Uribe, D., Ruiz, O.E., and Steeb, H.: Finite Difference Calculations of Permeability in Large Domains in a Wide Porosity Range. Archive of Applied Mechanics, 85, 1043-1054, doi:
10 10.1007/s00419-015-1025-4, 2015.

Regnet, J. P., P. Robion, C. David, J. Fortin, B. Brigaud, and B. Yven: Acoustic and reservoir properties of microporous carbonate rocks: Implication of micrite particle size and morphology: Journal of Geophysical Research Solid Earth, 120, 790–811, http://dx.doi.org/10.1002/2014JB011313, 2014.

Ringstad, C., Westphal, E., Mock, M., Al Hammadi, M., Al Ratrout, A and Kalam, Z.: Elastic Properties
15 of Carbonate Reservoir Rocks Using Digital Rock Physics: 75th EAGE Conference & Exhibition, London, Tu-01-02, 2013.

Saenger E.H., Gold N., and Shapiro, S. A.: Modeling the propagation of elastic waves using a modified finite-difference grid. Wave Motion, 31, 77-92, doi: 10.1016/S0165-2125(99)00023-2, 2000.

Saenger E.H., Madonna C., Osorno M., Uribe D. and Steeb H.: Digital Carbonate Rock Physics, SEG
20 Annual Meeting, Denver, Colorado, 2014.

Saenger E.H., Krüger, O.S. and Shapiro, S. A.: Numerical considerations of fluid effects on wave propagation: Influence of the tortuosity, Geophysical Research Letters, 31, L21613, doi: 10.1029/2004GL020970, 2004.

20

Saenger E.H., Lebedev M., Uribe D., Osorno M., Vialle, S., Duda, M., Inglauer S. and Steeb H.: Analysis of high resolution X-ray CT images of Bentheim sandstone under elevated confining pressure, Geophysical Prospecting, doi: 10.1111/1365-2478.12400, 2016.

Saenger E.H., Enzmann F., Keehm Y., and Steeb H.: Digital rock physics: Effect of fluid viscosity on
5   effective elastic properties. Journal of Applied Geophysics, 74, 236-241, doi: 10.1016/j.jappgeo.2011.06.001, 2011.

Scotellaro; C., Vanorio, T. and Mavko, G.: The effect of mineral composition and pressure on carbonate rocks. 77th Annual International Meeting, SEG, Expanded Abstracts, 1684–1689, 2004.

Ulm, F.-J., and Abousleiman, Y.:The nanogranular nature of shale: Acta Geotechnica, 1, 77– 88, doi:
10   10.1007/s11440-006-0009-5, 2006.

Vialle, S. and Lebedev, M.: Heterogeneities in the elastic properties of microporous carbonate rocks at the microscale from nanoindentation tests. SEG Technical Program Expanded Abstracts, 3279-3284, doi: 10.1190/segam2015-5885016.1, 2015.

Vialle, S.; Dvorkin, J. and Mavko, G.: Implications of pore microgeometry heterogeneity for the
15   movement and chemical reactivity of CO_2 in carbonates. Geophysics, 78, L69-L86, 2013.

Wang, Y., Y. Yang, T. Xiao, K. Liu, B. Clennell, G. Zhang, H. Wang, 2013, Synchrotron-Based Data-Constrained Modeling Analysis of Microscopic Mineral Distributions in Limestone: International Journal of Geosciences, 4, 344-351, doi: 10.4236/ijg.2013.42032, 2013.

Figures
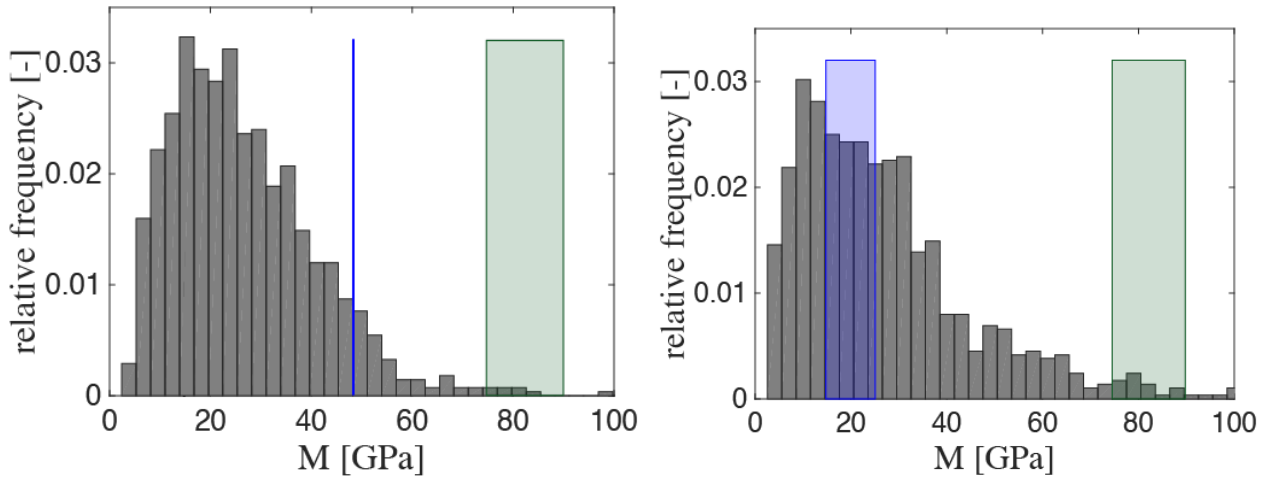
5   Fig. 1: Nano-Indentation results for *Carb-A* (left hand side) and *Carb-B* (right hand side). In blue we
illustrate the corresponding moduli range from ultrasonic experiments on dry samples from 0 to 30 MPa
confining pressure, and in green we illustrate the moduli range given by the solid anisotropic calcite
crystal. Overall we observe that the medium effective indentation module M is slightly stiffer for *Carb-*
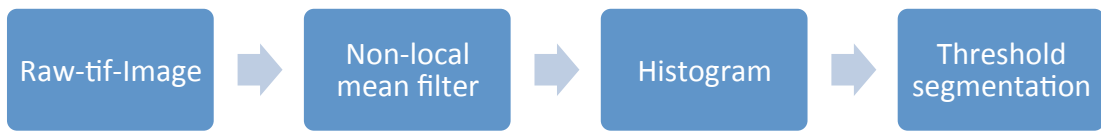*A* (26 GPa vs. 25 GPa).

10

Raw-tif-Image → Non-local mean filter → Histogram → Threshold segmentation

Fig. 2: Simplified segmentation workflow as applied in this study.
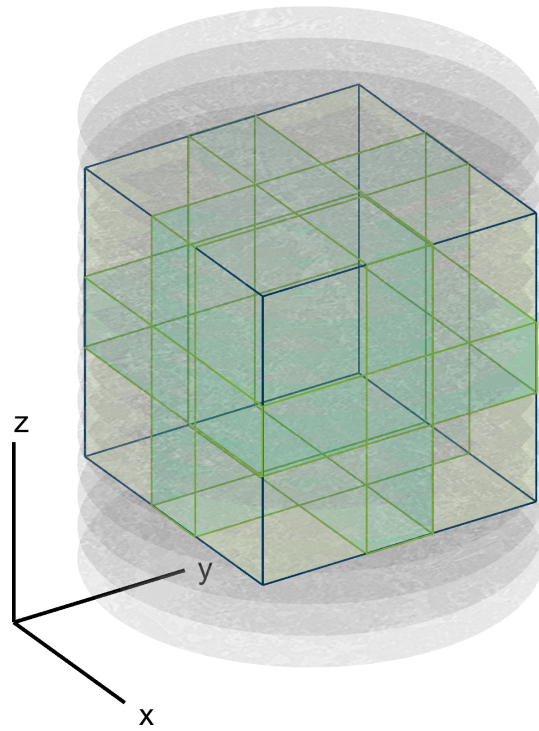
Fig. 3: Sketch to illustrate the segmentation geometry (here for *Carb-B*; high-resolution). The full cube is subdivided into eight partly intersecting <mark>subvolumes</mark> with a size of 400^3 gridpoints. Those <mark>subvolumes</mark> are used in the numerical simulations to estimate effective material properties.

5

24
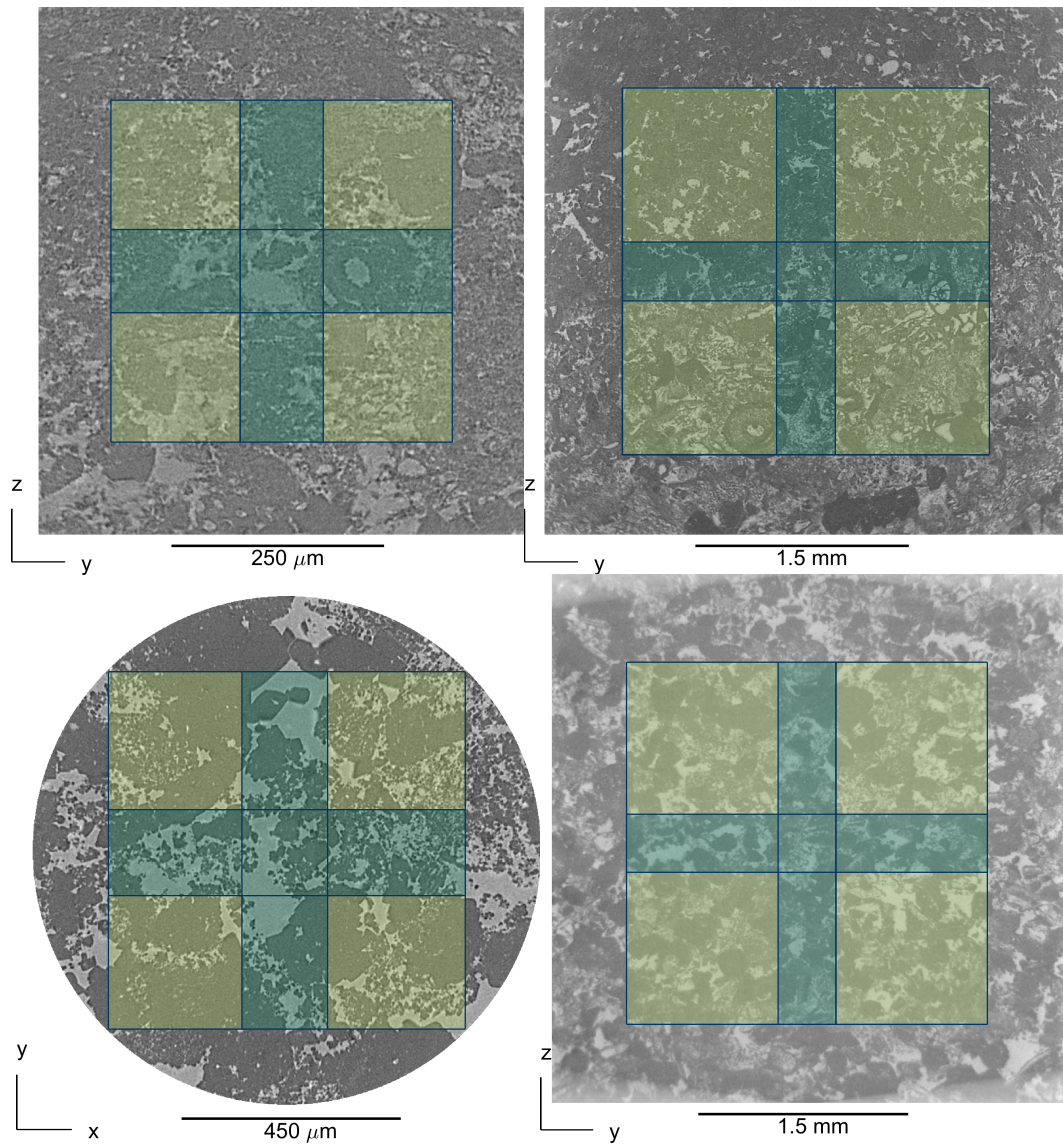
5

Fig. 4: Slices of the raw tiff-images of the scanned samples. <mark>The dark green areas mark the overlapping zones of the considered subvolumes.</mark> Top row: *Carb-A* with high (left) and low resolution (right). Bottom row: *Carb-B* with high (left) and low resolution (right).
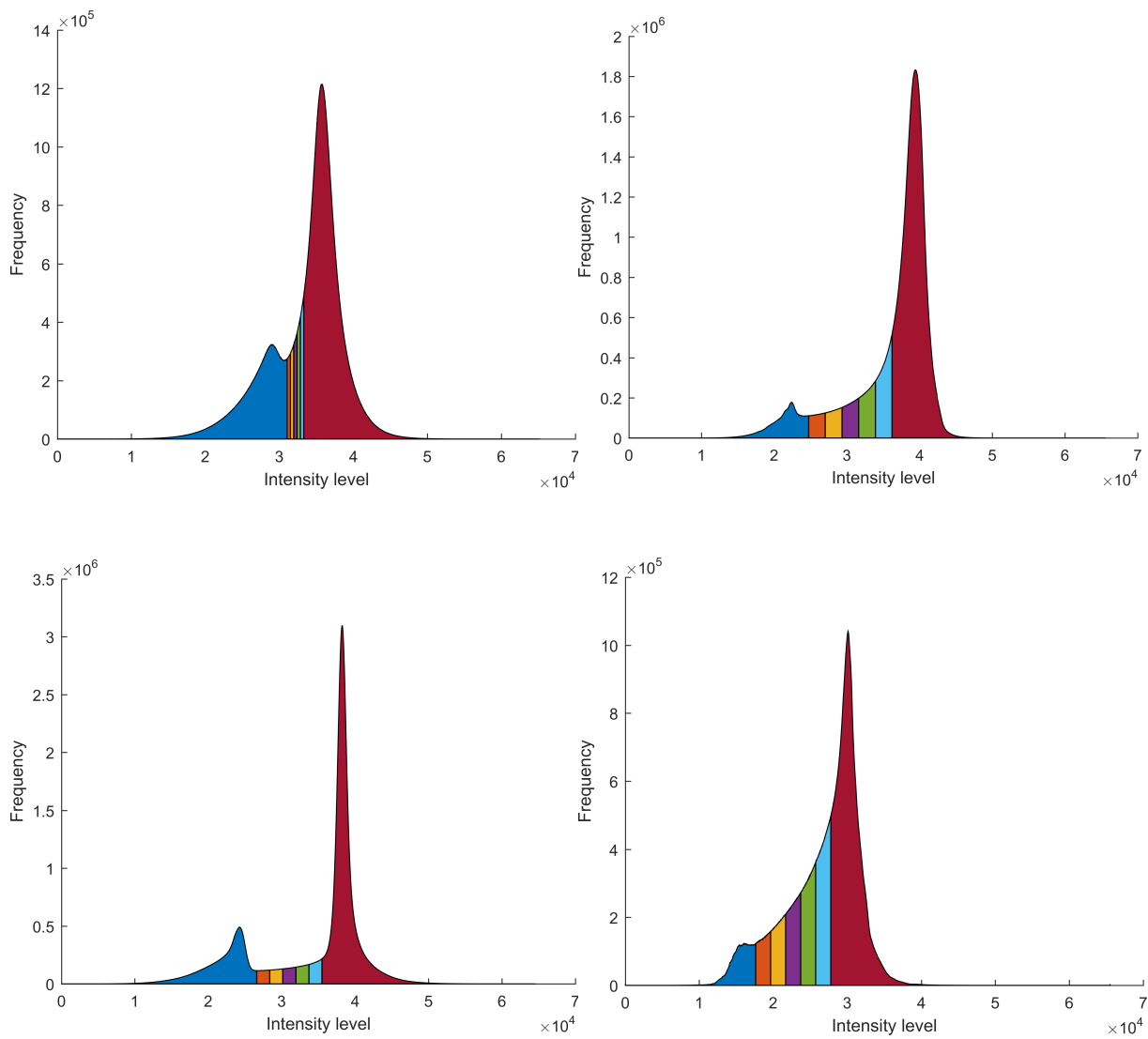
5   Fig 5.: Color-coded histograms of the scanned samples. Top row: *Carb-A* with high (left) and low resolution (right). Bottom row: *Carb-B* with high (left) and low-resolution (right). Between the high-confidence pore phase (marked blue) and the high-confidence mineral phase (marked red) we define five intermediate classes to characterize the micritic phases within carbonate rock.

10

26
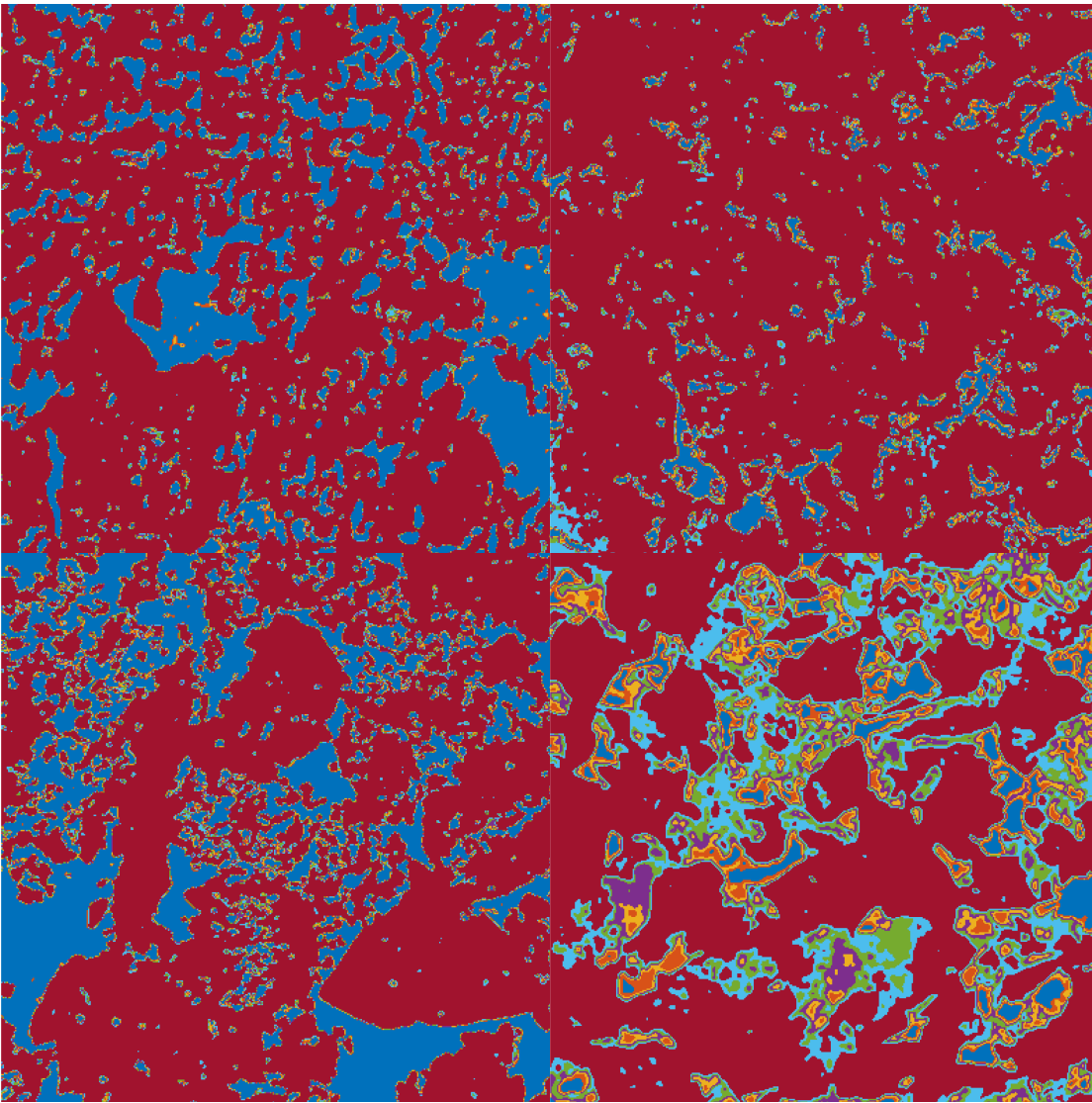
Fig 6: Slices of the segmented images used for the numerical simulations to determine permeability and velocities. Top row: *Carb-A* with high (left) and low-resolution (right). Bottom row: *Carb-B* with high (left) and low resolution (right).
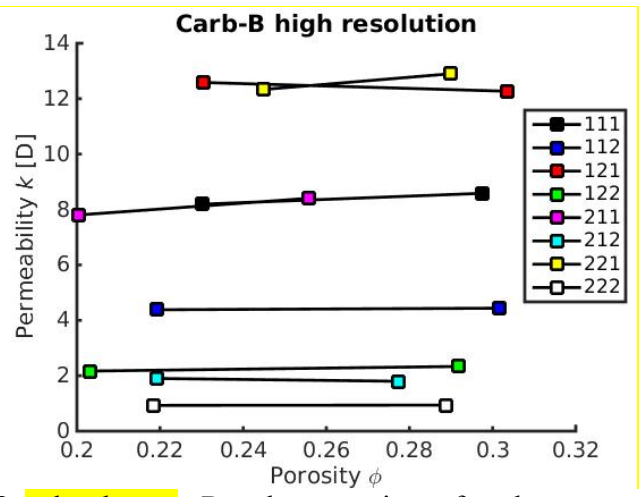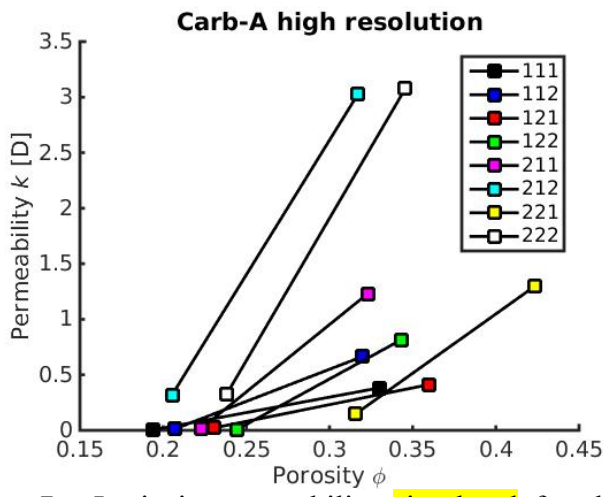
Fig. 7: Intrinsic permeability simulated for the 8 subvolumes. Results are given for the extreme porosities configuration of *Carb-A* (left hand side) and *Carb-B* (right hand side) high resolution samples.
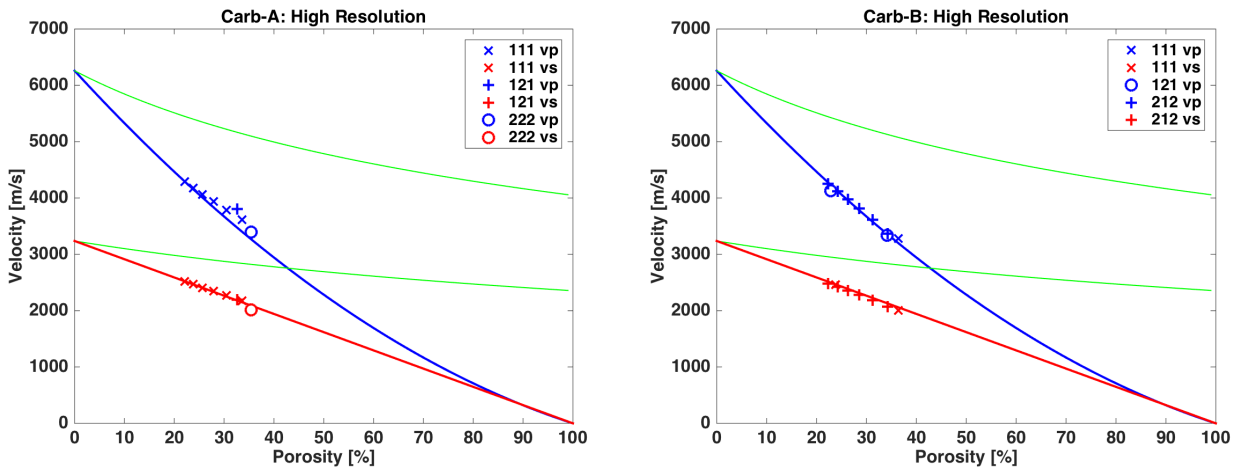
5

28

Fig. 8: Effective P- and S-wave velocities (red and blue dots, respectively) for simulations based on a two-phase segmentation. The results were obtained for a random selection of subvolumes of *Carb-A* (left hand side) and *Carb-B* (right hand side). The blue and red lines are the velocity trends given by equations (4) and (5). The green lines are derived by using the upper Hashin-Shtrikman bounds. For details please refer to the text.
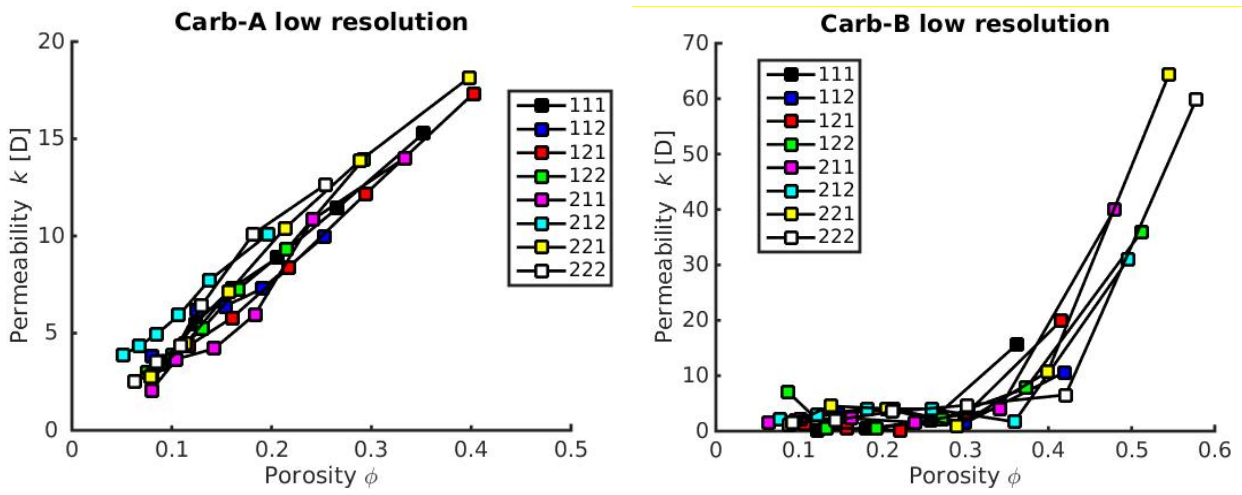
29

Fig. 9: Simulated intrinsic permeability as a function of porosity. Results for the 8 subvolumes of *Carb-A* (left hand side) and *Carb-B* (right hand side) low-resolution samples. Squares markers display each of the pore-solid configurations.
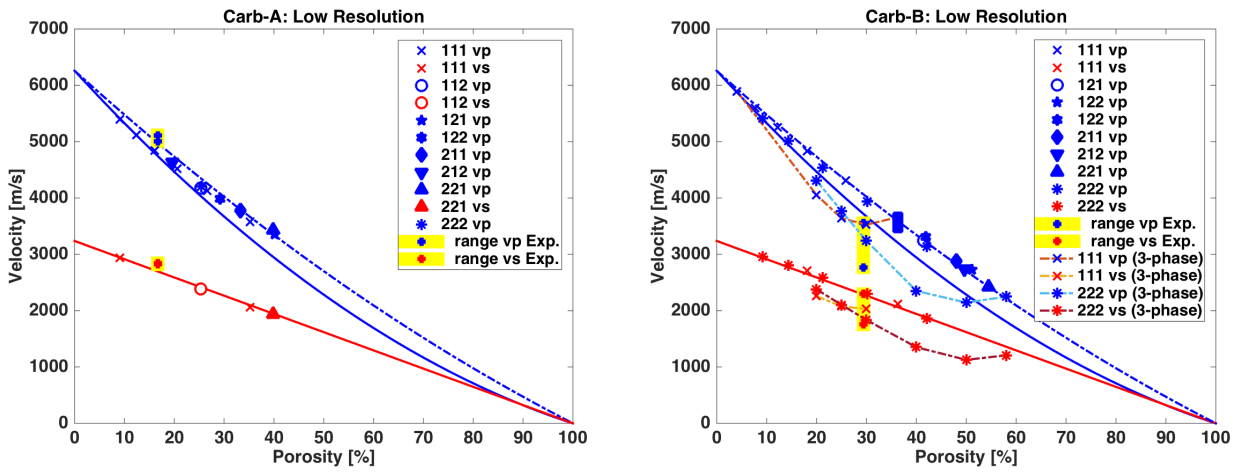
Fig 10: Effective P-wave and S-wave velocities (red and blue dots, respectively) for simulations based on a two-phase segmentation. The results were obtained for subvolumes of the low-resolution images of *Carb-A* (left hand side) and of *Carb-B* (right hand side). The blue and red lines are the velocity trends given by equations (4) and (5); the blue dashed-dotted line is the trend given by equation (6). The experimental results (interval from 0 to 30 MPa confining pressure) are illustrated with crosses connected with yellow bars for comparison. The green dots display the results of the multi-phase simulations (only performed for *Carb-B* and for P-waves). For details please refer to the text.
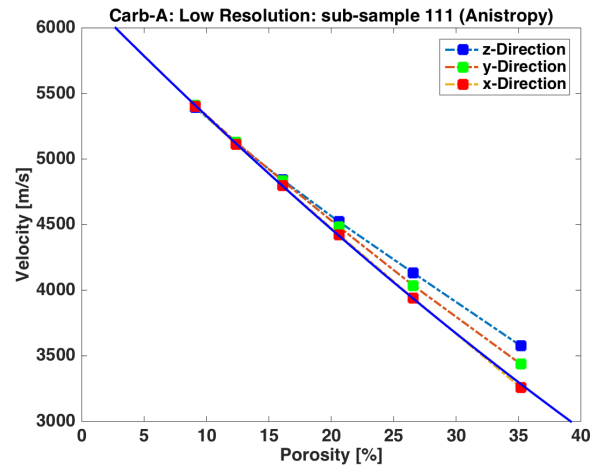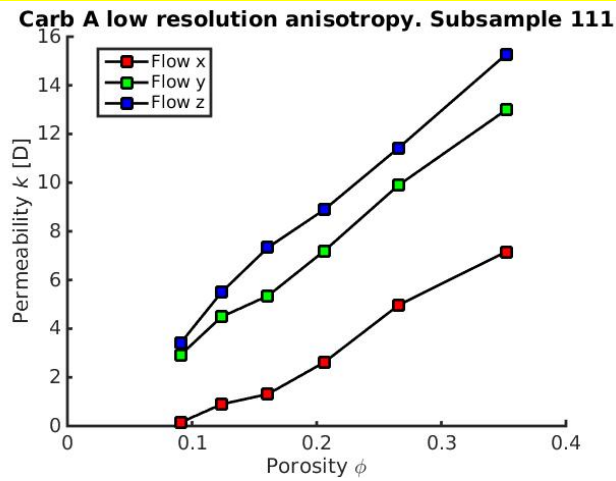
31

Fig. 11: Left hand side: intrinsic permeability for subvolume 111 of *Carb-A* low resolution. Permeability calculated from flow simulated in X, Y and Z directions. Right hand side: P-wave velocities for all propagation directions of the same sup-sample. The solid line is the velocity trend given by equation (4). The moderate anisotropy visible in permeability is not present for the velocities.

Tables

Table 1: Helium bulk and grain density (in g/cm^{-3}), helium porosity (in PU) and air-permeability (in mD) measured at benchtop conditions, for *Carb-A* and *Carb-B*. Permeability of plug *Carb-A* is below the sensitivity level of the apparatus used (0.1 mD). Values are from Vialle et al. (2013).

Sample ID	Porosity	Bulk density	Grain density	Permeability
Carb-A	0.167 ± 0.002	2.24 ± 0.01	2.69 ± 0.01	< 0.1
Carb-B	0.294 ± 0.003	1.90 ± 0.01	2.70 ± 0.01	60 ± 5

5

33

Table 2: Pressure dependence of the elastic-wave velocities for the two studied samples. Pressure is in megapascal, and P- and S-wave velocity are in kilometers per second. Values are from Vialle et al. (2013).

Pressure	Carb-A		Carb-B	
	Vp	Vs	Vp	Vs
0	5.007	2.835	2.769	1.754
2.5	5.045	2.838	3.295	2.032
7.5	5.091	2.835	3.477	2.191
10	5.100	2.834	3.504	2.226
20	5.116	2.822	3.551	2.295
30	5.113	2.821	3.553	2.290
25	5.114	2.821	3.548	2.284
15	5.085	2.822	3.527	2.268
5	5.048	2.840	3.384	2.195
0	5.033	2.842	2.792	1.785

5

Table 3: CT-scanner parameters used for image acquisition of the two carbonate samples. Sample abbreviations are explained in Table 1.

Pressure	Carb-A		Carb-B	
	Low resolution	High resolution	Low resolution	High resolution
Voxel size	$(3.4348 \ \mu m)^3$	$(0.6245 \ \mu m)^3$	$(3.4352 \ \mu m)^3$	$(1.1450 \ \mu m)^3$
Image size	1012 * 1012	1012 * 1012	1013 * 1013	1013 * 1013
Acceleration voltage	60 kV	60 kV	60 kV	60 kV
Current	80 μA	80 μA	83 μA	83 μA
Source-to-sample distance	50.00 mm	11.10 mm	12.00 mm	12.00 mm
Detector-to-sample distance	50.00 mm	120.00 mm	12.00 mm	60.00 mm
Exposure time	20 s	20 s	1 s	6 s
Optical magnification	4X	4X	4X	4X

5